Clim. Past Discuss., https://doi.org/10.5194/cp-2019-31
Manuscript under review for journal Clim. Past
Discussion started: 7 March 2019


# Glacial $CO_2$ decrease and deep-water deoxygenation by iron fertilization from glaciogenic dust

Akitomo Yamamoto[1,2], Ayako Abe-Ouchi[1,2], Rumi Ohgaito[1], Akinori Ito[1], Akira Oka[2]

[1]Japan Agency for Marine-Earth Science and Technology, Yokohama, Japan
[2]Atmospheric an Ocedn Research Institute, The University of Tokyo, Kashiwa, Japan

*Corresponding author*: A. Yamamoto (akitomo@jamstec.go.jp)

**Abstract**

**Increased accumulation of respired carbon in the deep ocean associated with enhanced efficiency of the biological carbon pump is thought to be a key mechanism of glacial $CO_2$ drawdown. Despite greater oxygen solubility due to sea surface cooling, recent quantitative and qualitative proxy data show glacial deep-water deoxygenation, reflecting increased accumulation of respired carbon. However, the mechanisms of deep-water deoxygenation and contribution from the biological pump to glacial $CO_2$ drawdown have remained unclear. In this study, we report the significance of iron fertilization from glaciogenic dust for glacial $CO_2$ decrease and deep-water deoxygenation using our numerical simulation, which successfully reproduces the magnitude and large-scale pattern of the observed oxygen changes from the present to Last Glacial Maximum. Sensitivity experiments reveal that physical changes (e.g., more sluggish ocean circulation) contribute to only half of all glacial deep deoxygenation, whereas the other half is driven by enhanced efficiency of the biological pump. We found that iron input from the glaciogenic dust with higher iron solubility is the most significant factor for enhancement of the biological pump and deep-water deoxygenation. Glacial deep-water deoxygenation expands the hypoxic waters in the deep Pacific and Indian Ocean. The simulated global volume of hypoxic waters is nearly double the present value, which suggest that the glacial deep-water is sever environment for the benthic animals. Our model underestimated the deoxygenation in the deep Southern Ocean due to enhanced ventilation. The model-proxy comparison of oxygen change suggest that the stratified Southern Ocean is required for reproducing oxygen decline in the deep Southern Ocean. Enhanced efficiency of biological pump contributes to**

Clim. Past Discuss., https://doi.org/10.5194/cp-2019-31
Manuscript under review for journal Clim. Past
Discussion started: 7 March 2019


**decrease of glacial $CO_2$ by more than 30 ppm, which is supported by the model-proxy agreement of oxygen change. Our findings confirm the significance of the biological pump in glacial $CO_2$ drawdown and deoxygenation.**

## 1 Introduction

The oceanic carbon cycle has been proposed as a driver of glacial–interglacial $CO_2$ change; however, the magnitude of glacial $CO_2$ reduction of 80-100 ppm has yet to be fully reproduced by numerical model simulations using both an ocean general circulation model (OGCM) and a biogeochemical model (Ciais et al., 2013). The oceanic biological carbon pump, by which the photosynthetic production, sinking, and remineralization of organic matter store dissolved inorganic carbon in the deep ocean, is one of the mechanisms controlling glacial-interglacial $CO_2$ change, as well as future atmospheric $CO_2$ change (Sarmiento and Gruber 2006; Sigman et al., 2010; Yamamoto et al., 2018). During the glacial periods, the efficiency of the biological pump would have been enhanced by biogeochemical processes (e.g., dust-borne iron fertilization (Martin, 1990) and increase in nutrient inventory associated with sea-level drop (Broecker, 1982; Wallmann et al., 2016) and thus, atmospheric $CO_2$ would have been transported to the glacial deep ocean. Although changes in marine productivity during glacial periods and its relationship to the dust deposition flux have been widely supported by the proxy records (Kohfeld et al., 2005; Jaccard et al., 2013), there were no direct proxy records of greater accumulation of respired organic carbon. Thus, the contribution of the biological pump on glacial $CO_2$ reduction is poorly understood.

Because the dissolved oxygen cycle is the mirror image of the biological carbon cycle (oxygen is produced by photosynthesis and is utilized with consistent stoichiometry through the remineralization of sinking organic matter in the ocean interior), oxygen is consumed in the ocean interior when respired organic carbon is accumulated into the seawater. Thus, reconstructed oxygen change is useful for constraining the magnitude of the biological pump and accumulation of respired carbon. Proxy data show that, despite greater oxygen solubility due to lower sea surface temperatures (SSTs), oxygen concentrations decreased throughout the deep ocean during the Last Glacial Maximum (LGM) (Jaccard and Galbraith, 2012). This indicates greater oxygen consumption and accumulation of respired carbon, which could have been caused by several processes: greater transport of organic matter into the deep ocean, more restricted air-sea exchange due to sea-ice expansion, and/or more sluggish ocean circulation. However, previous modeling studies display conflicting oxygen changes in the LGM simulations (Galbraith and Jaccard, 2015; Buchanan et al., 2016; Bopp et al., 2017; Galbraith and de Lavergne, 2018), and the causes of oxygen decline in the deep ocean have not yet been fully explored.

Furthermore, because most observations provide only qualitative estimates of oxygen changes, previous model-proxy comparisons discussed only the glacial oxygen trend (oxygenation in the upper ocean and deoxygenation in the deep ocean). Several recent studies using $\delta^{13}C$ in benthic foraminiferal or iodine-to-calcium ratios in planktonic foraminifera, were able to quantify changes in oxygen concentration (Hoogakker et al., 2015, 2018; Umling and Thunell, 2018; Gottschalk et al., 2016; Lu et al., 2016; Bunzel et al., 2017; Schmiedl and Mackensen, 2006). These quantitative proxy data provide firmer constraints on accumulation of respired carbon, such that quantitative model-proxy comparison of oxygen change is very useful for quantifying the contribution of the biological pump to glacial $CO_2$ drawdown.

In this study, to quantify the impact of changes in the biological pump on the glacial carbon and oxygen cycles, we conducted pre-industrial (PI) and LGM simulations using the coupled atmosphere–ocean general circulation model (Oka et al., 2011), aerosol model (Ohgaito et al., 2018), and ocean biogeochemical model (Yamamoto et al., 2015). We focus here on the iron fertilization process for enhancing the biological pump. Our new attempt is to quantify iron fertilization effects from desert dust and glaciogenic dust (derived from glacier erosion), separately. Previous studies using mineral aerosol models suggest that glaciogenic dust significantly contributes to an increase in dust deposition flux at high latitudes during the LGM (e.g., the glaciogenic dust derived from Patagonian glaciers increases dust deposition in the Southern Ocean (SO)) and provides a LGM dust deposition flux distribution more consistent with the reported measurements (Mahowald et al., 2006; Ohgaito et al., 2018). Moreover, the solubility of iron in glaciogenic dust (~3%) is much higher than that in desert dust (~1%) (Schroth et al., 2009), but the higher solubility effect of glaciogenic dust on the iron fertilization was not considered in previous modeling studies. Glaciogenic dust supply bioavailable iron significantly (Shoenfelt et al., 2018) and would therefore have a large impact on biological productivity in high nutrient and low chlorophyll (HNLC) regions where biological productivity is limited by lack of iron. We also consider the effect of an increase in macronutrients inventory associated with glacial sea level drop of ~120 m (Broecker, 1982; Wallmann et al., 2016). Decrease in area of continental margins reduces the burial of organic matter in margin sediments, thus leading to increases in global inventory of phosphate ($PO_4$) and nitrate ($NO_3$). Based on a recent simulation, increases in $NO_3$ and $PO_4$ inventories by 15% are assumed (Wallmann et al., 2016).

We performed several sensitivity experiments listed in Table 1 to explore the contribution of changes in atmospheric dust and nutrient inventory on glacial carbon and oxygen cycles. Moreover, our modeled oxygen changes are compared to recently reported qualitative (Jaccard and Galbraith, 2012) and quantitative reconstructions (Hoogakker et al., 2015, 2018; Gottschalk et al., 2016; Lu et al., 2016; Bunzel et al., 2017; Umling and Thunell, 2018; Schmiedl and Mackensen, 2006) to evaluate the simulated accumulation of respired carbon. Our simulation show that enhanced efficiency of biological pump associated with glaciogenic dust and increased nutrient inventory plays a crucial role in the glacial $CO_2$ decrease and deep-water deoxygenation.

## 2 Model and experiments

The ocean biogeochemical cycle was calculated by the MIROC-based offline biogeochemical model, based on Yamamoto et al. (2015), with the implementation of an iron cycle. A one box atmosphere is coupled to an offline biogeochemical model in order to predict atmospheric $CO_2$ concentration through gas exchange between the atmosphere and ocean surface. For the tracer calculation, the model uses prescribed monthly output data of horizontal ocean velocities, vertical diffusivity, temperature, salinity, sea surface height, sea surface wind speed, sea-ice fraction, and sea surface solar radiation, derived from PI and LGM simulations conducted by Oka et al. (2011) using the MIROC 4m AOGCM. Both PI and LGM simulations follow the PMIP2 protocol (Braconnot et al., 2007). MIROC 4m simulates the weaker and shallower AMOC at the LGM (see Fig. 1 in Oka et al. (2011)), which is consistent with $\delta^{13}C$ distributions reported from proxy data (Curry and Oppo, 2005). The horizontal and vertical resolutions of offline biogeochemical model are the same as in MIROC 4m.

This biogeochemical model includes two phytoplankton classes (nitrogen fixers and other phytoplankton), zooplankton, particulate detritus, nitrate ($NO_3$), phosphate ($PO_4$), dissolved iron (DFe), dissolved oxygen ($O_2$), dissolved inorganic carbon (DIC), alkalinity (ALK), two carbon isotopes ($^{13}C$ and $^{14}C$), and an ideal age tracer. The ideal age is set to zero at the surface and ages at a rate of 1 yr $yr^{-1}$ in the ocean interior. Constant stoichiometry relates the C, N, P, and DFe content of the biological variables and their exchanges to inorganic variables ($NO_3$, $PO_4$, DFe, $O_2$, ALK, and DIC). The maximum phytoplankton growth and microbial remineralization rates are assumed to increase with seawater temperature (Eppley, 1972). The iron cycle that is

incorporated in the biogeochemical model mainly follows Parekh et al (2005). Dust deposition, sedimentary fluxes, and hydrothermal fluxes are considered as DFe sources. To obtain a realistic distribution of the iron limited region, total ligand concentration which controls the amount of the free form of iron is set to a global constant value of 0.6 μmol $m^{-3}$ instead of the original value of 1 μmol $m^{-3}$ (Fig. 1a).

Dust deposition flux is obtained from monthly output data of MIROC-ESM in PI and LGM simulations (Ohgaito et al., 2018). Dust is assumed to contain a constant fraction of iron (3.5 wt%), and 1% of the iron in desert dust is assumed to dissolve instantaneously at the sea surface. The global DFe flux from dust in the PI is 2.7 Gmol $yr^{-1}$ (Table 1). We used two sets of LGM dust deposition flux labelled as LGMctl and LGMglac that were calculated in a previous study (Ohgaito et al., 2018). LGMctl is the standard LGM simulation, which has been submitted to CMIP5/PMIP4. LGMglac is identical to LGMctl, except that additional glaciogenic dust flux based on Mahowald et al (2006) was included. In LGMctl, the dust deposition flux is underestimated in North America, Eurasia, the South Pacific, the SO, and Antarctica compared to proxy data of ice and sediment cores (Kohfeld et al., 2013; Albani et al., 2014). Since glaciogenic dust increases dust deposition at high latitudes, the underestimation is generally improved in LGMglac (see Ohgaito et al., 2018, for more details). The global DFe fluxes from dust are 8.6 Gmol $yr^{-1}$ and 13.9 Gmol $yr^{-1}$ for LGMctl and LGMglac, respectively. In LGM_glac3%, iron solubility of 3% in glaciogenic dust is assumed (Schroth et al., 2009), so that the global DFe flux is 24.5 Gmol $yr^{-1}$. As with the present DFe input from dust, glacial DFe input has large uncertainties. Thus, as an upper estimate of the DFe flux from dust, we set the iron solubility of 10% in glaciogenic dust in LGM_glac10%. This assumption is consistent with ice core data of EPICA Dome C from East Antarctica (Conway et al., 2015). In present days, wider range of aerosol Fe solubility (from 0.2% to 48%) has been derived from observations over the Southern Ocean, but different types of Fe-containing minerals such as pyrogenic Fe oxides could be considered to achieve the high Fe solubilities (Ito et al., 2019).

DFe input flux from the sediments is estimated based on Moore and Braucher (2008). We assumed that sedimentary DFe flux is proportional to the flux of organic carbon reaching the sea floor. In order to consider the realistic bathymetry of the continental shelves, the iron flux is weighted by the fraction of bottom area of ETOPOV2 data that falls within the bounds of

the model grid cell. The global DFe flux from the sediments in the PI is 33.1 Gmol $yr^{-1}$. In LGM simulations, DFe input from sedimentary sources changes according to the flux of organic carbon reaching the sea floor. A decrease in DFe input from sedimentary sources due to sea-level drop is not considered. The hydrothermal DFe flux is regulated by the ridge spreading rate, as parameterized by a constant DFe/Helium ratio (Tagliabue et al., 2010). The hydrothermal DFe flux in the PI is ~8.5 Gmol $yr^{-1}$. In LGM simulations, DFe input from hydrothermal sources is not changed from PI.

The biogeochemical model was initialized from the annual mean climatology data based on the World Ocean Atlas 2009 (WOA2009: Garcia et al., 2010a and 2010b) for dissolved $NO_3$, $PO_4$, and $O_2$ and the Global Ocean Data Analysis Project (Key et al., 2004) for DIC and ALK. The initial concentration of DFe is a constant value of 0.6 nM. For the spin-up, the last 50 years of data in the MIROC PI experiments are cyclically applied to the offline ocean biogeochemical model. The model was spun up for more than 3000 years with prescribed atmospheric $CO_2$ concentration of 285 ppm in order to eliminate model drift in the global inventory of all tracers. Similar to Yamamoto et al (2015), all physical and biogeochemical tracers, except salinity and dissolved iron, have correlation coefficients with observational data of more than 0.85 and normalized standard deviation values between 0.7 and 1.1.

LGM experiments were run for 3000 years, following 3000 years spin-up under PI conditions. Atmospheric $CO_2$ concentration is predicted. We increased salinity, $PO_4$, and $NO_3$ inventory by 3% in the first year of simulations to account for reduced ocean volume due to sea level drop. All experiments are listed in Table 1. LGM_clim uses LGM boundary conditions. LGM_dust is based on LGM_clim but use dust deposition flux of LGMctl. Similarly, LGM_glac3% and LGM_glac10% use dust deposition flux of LGMglac, but with an iron solubility of glaciogenic dust of 3% and 10%, respectively. LGM_all is similar to LGM_glac3%, but $NO_3$ and $PO_4$ inventories are increased by 15%. This assumption is based on a recent model simulation that shows ~15% increase in nutrients inventory is caused by reduced burial of organic matter in shallow sediments associated with sea level drop (Wallmann et al., 2016). We analyzed the results from the last 100 years of each simulation.

## 3 Results and Discussion

### 3.1 Glacial nutrient cycles and export production

In the LGM_clim, which uses LGM climate boundary conditions, the redistribution of $NO_3$ induced by weaker and shallower Atlantic meridional overturning circulation (AMOC) reduces nutrient supply from the deep ocean to the surface (Table 2 and Fig. 2). $NO_3$ concentration in the euphotic zone decreases by 12%, and the global export production (EP) is reduced by 0.54 Pg C $yr^{-1}$ compared with the PI simulation. Corresponding to the surface $NO_3$ decrease, significant EP decreases are found in the North Atlantic and North Pacific (Fig. 3a and Fig. S1). On the other hand, surface dissolved iron (DFe) concentration changes slightly. Since these changes in DFe and $NO_3$ shrink the iron-limited areas by 27% (Fig. 1b), the simulated LGM climate tends to mitigate the impacts of iron fertilization on biological productivity and the carbon cycle.

To evaluate the impacts of desert and glaciogenic dust on the ocean biogeochemical cycles, we conducted sensitivity studies. The DFe input from desert dust with 1% iron solubility is applied in LGM_dust, whereas glaciogenic dust with 3% or 10% iron solubility is additionally applied in LGM_glac3% or LGM_glac10%, respectively. Iron fertilization from only desert dust have a limited impact on EP because dust deposition flux of the Southern Ocean is underestimated in LGM_dust. Iron fertilization from both desert and glaciogenic dust increases EP by 0.88 Pg C $yr^{-1}$ in the south of 45°S with iron limitation, whereas EP decreases by 0.86 Pg C $yr^{-1}$ in the north of 45°S, where most oceans are nitrogen-limited regions (LGM_glac3% – LGM_clim; Table 2). Enhanced primary production consumes $NO_3$ of the euphotic zone in the SO and its anomaly is transported to the Antarctic bottom water (AABW). Subsequently, the reduction of surface $NO_3$ in the SO is also transported to low-latitude regions via surface and intermediate waters (Fig. 2), thus reducing EP in nitrogen-limited regions at the low latitudes. Remarkable EP reductions occur in the north of the iron-limited regions of the SO (Fig. 3b). Our results demonstrate that enhanced biotic carbon export in the SO is partly compensated for by reduced carbon export in the low-latitude regions. From the comparison between the effect of desert dust (LGM_dust – LGM_clim) and that of glaciogenic dust (LGM_glac3% – LGM_dust), we found that an increase in export production due to dust-bone iron fertilization in the SO is mainly caused by glaciogenic dust (Table 2).

Under 15% increases in $NO_3$ and $PO_4$ inventory associated with sea level drop (LGM_all), EP is increased globally in the nitrogen-limited regions, leading to global EP increase by 0.86 Pg C $yr^{-1}$ (LGM_all – LGM_glac3%; Table 2). Simulated EP changes from PI are in good agreement with the paleoproductivity reconstruction (Kohfeld et al., 2005) (Fig. 3c). One of the common patterns is the north-south dipole pattern in the SO with decrease of EP at higher-latitudes and increase of EP at lower-latitudes. EP decrease at higher latitudes is attributed to the expansion of sea ice and associated reduction of surface shortwave (Oka et al., 2011), whereas iron fertilization increases EP at lower latitudes. On the other hand, EP changes also have an east-west dipole pattern; both the proxy data and model show no significant changes of EP in the South Pacific Ocean and clear EP increases in the South Atlantic and Indian Oceans. We found that this pattern is attributed to iron fertilization by glaciogenic dust. Glaciogenic dust derived from Patagonian glaciers is transported to the South Atlantic and Indian Oceans by the southern westerly wind, but is unable to reach the South Pacific (Fig. S2). The realistic distribution of glaciogenic dust deposition simulated by an aerosol model and our consideration of its higher iron solubility enable us to reproduce the east-west dipole pattern of EP changes.

### 3.2 $CO_2$ reduction and its relationship to efficiency of the biological pump and dust flux

Climate change reduces the atmospheric $CO_2$ concentration by 26.4 ppm (LGM_clim – PI, Table 2), which is similar to previous simulations (Chikamoto et al, 2012; Kobayashi et al., 2015). Circulation changes (i.e., weaker and shallower AMOC and expansion of AABW) cause dissolved inorganic carbon (DIC) to decrease in the upper ocean and increase below 2000 m, so that the vertical DIC gradient between the surface and deep oceans is enhanced (Fig. 4). The efficiency of the oceanic biological pump is calculated following Ito and Follows (2005). Global mean preformed $PO_4$ is the difference between total globally averaged $PO_4$ and global mean remineralized $PO_4$, $P_{pref} = P_{tot} - P_{remi}$. Here $P_{pref}$ is preformed $PO_4$ concentration, $P_{tot}$ is the total $PO_4$ concentration, and $P_{remi}$ is remineralized $PO_4$ concentration. The remineralized $PO_4$ is given by $P_{remi}$=AOU × $R_{P:O}$, where $R_{P:O}$ is a constant phosphorous to oxygen ratio. Decrease in preformed $PO_4$ and thus increase in remineralized $PO_4$ indicate the increase in the efficiency of the oceanic biological pump. Although globally integrated EP decreases, circulation change and deepening of the remineralization profile due to seawater cooling (Matsumoto, 2007) reduce the preformed nutrient

inventory and thus enhance the efficiency of the biological pump (Table 2). The enhanced accumulation of respired carbon associated with a more efficient biological pump and increased $CO_2$ solubility from lower SST contribute to decreased $CO_2$.

Iron fertilization from desert dust and glaciogenic dust enhance the vertical DIC gradient and cause $CO_2$ reduction of 1.2 ppm (LGM_dust – LGM_clim) and 15.6 ppm (LGM_glac3% – LGM_dust), respectively. Our results show that the glacial $CO_2$ reduction due to dust-bone iron fertilization is mainly driven by glaciogenic dust. Simulated total $CO_2$ reduction of 16.8 ppm induced by iron fertilization is in the range of previous studies using OGCM (8-25 ppm $CO_2$ drawdown (Bopp et al., 2003; Parekh et al., 2006; Tagliabue et al., 2009; Oka et al., 2011; Lambert et al., 2015; Muglia et al., 2017). DFe supply from dust also contributes to glacial $CO_2$ reduction through enhancing the efficiency of the biological pump (Table 2). The simulated atmospheric $CO_2$ concentration is reduced proportionally to the preformed $PO_4$ (Fig. 5a), similar to previous simulations under the present climate (Ito and Follows, 2005; Marinov et al., 2008). Figure 5b shows $CO_2$ change in response to the magnitude of DFe input. The efficiency of iron fertilization to reduce $CO_2$ decreases with increasing DFe flux. This nonlinear response is driven by decrease in iron-limited areas and the associated weakening of the effect of iron on EP (Fig. 5c). Since the iron-limited region shrinks dramatically and $CO_2$ difference between LGM_glac3% and LGM_glac10% is small, $CO_2$ reduction of 20 ppm in LGM_glac10% is close to the upper limit (i.e., there are no iron-limited regions and thus no additional $CO_2$ reduction).

Increases in nutrient inventory from lower sea levels drive additional $CO_2$ drawdown by 16 ppm (LGM_all – LGM_glac3%). We found that changes in the biological pump induced by iron fertilization and an increase in nutrient inventory contribute to glacial $CO_2$ decline by more than 30 ppm. The resulting total $CO_2$ reduction is ~60 ppm, which our model does not reproduce as the full variation of glacial-interglacial $CO_2$ change. Note that the carbonate compensation process is not considered in our simulation. The simulated increase in the bottom water DIC (Fig. 4) would enhance dissolution of calcium carbonate in the sediments and thereby increase ocean alkalinity, leading to further $CO_2$ decline (Bouttes et al., 2011; Brovkin et al., 2012; Kobayashi et al., 2018). In the next section, to assess the simulated accumulation of respired carbon, we compare the simulated oxygen changes with qualitative and quantitative proxy records.

### 3.3 Model-proxy comparison of glacial oxygen changes

Compared with the compilation of qualitative and quantitative proxy records of oxygen change from the Holocene to Last Glacial Maximum, LGM_clim shows the increase in oxygen for the entire SO and underestimates deoxygenation in the deep Pacific and Indian Ocean, which is in contrast to proxy records (Fig. 6a). On the other hand, LGM_all successfully reproduces large-scale spatial patterns of oxygen change, including the SO (Fig. 6b). Moreover, the simulated changes in oxygen concentration are in good agreement with quantitative reconstructions: 45-65 mmol $m^{-3}$ decrease in the deep North Atlantic (Hoogakker et al., 2015), ~30-80 mmol $m^{-3}$ decrease in the eastern equatorial Pacific (Hoogakker et al., 2018; Umling and Thunell, 2018), and >80 mmol $m^{-3}$ in the upper SO of the Pacific sector (Lu et al., 2016). Our results clearly show the importance of the enhanced biological pump associated with iron fertilization and increase in nutrient inventory for global deep deoxygenation. These model-proxy agreements of oxygen change support the simulated $CO_2$ decrease of 30 ppm by the biological pump. However, reconstructed $O_2$ decrease of ~175 mmol $m^{-3}$ in the deep SO (Gottschalk et al., 2016) is much larger than the simulated decrease of ~30 mmol $m^{-3}$ from LGM_all, which means that the accumulation of respired carbon in the deep SO is underestimated in our model. This is the one reasons why the glacial-interglacial $CO_2$ change of ~100 ppm cannot be reproduced in our simulations.

To clarify the mechanism of $O_2$ change from LGM_all – PI, we decomposed the $O_2$ change into changes in saturation ($O_{2sat}$) and apparent oxygen utilization (AOU), whehre $\Delta O_2 = \Delta O_{2sat} - \Delta AOU$. The $O_{2sat}$ is computed from simulated seawater temperature and salinity, and AOU is calculated by subtracting the $O_2$ concentration from $O_{2sat}$. Ocean cooling increases $O_{2sat}$ globally, increasing the global mean value by 25.5 mmol $m^{-3}$ (Fig. 7a). As with $O_2$ change, ΔAOU shows the contrast between the upper and deep oceans (Fig. 7b). At depth of 0-800 m, the AOU decreases by 5.2 mmol $m^{-3}$ in north of 45°S, which results from the decrease in biological oxygen consumption associated with EP reduction and increased ventilation (Fig. 7f). Therefore, the combined effects of $O_{2sat}$ increase and AOU decrease contribute to overall $O_2$ increase in the upper ocean. In the deep ocean (>2 km), the sum of AOU increases by 72.8 mmol $m^{-3}$ (LGM_all in Table 2), which overcomes the $O_{2sat}$ increase,

resulting in deep $O_2$ depletion. The relationship between changes in $O_2$ concentration, $O_{2sat}$, and AOU are consistent with a previous simulation (Bopp et al., 2017).

The ΔAOU is also decomposed into effects of climate change (LGM_clim – PI), iron fertilization (LGM_glac3% – LGM_clim) and increase in nutrient inventory (LGM_all – LGM_glac3%). The effects of climate change, circulation change, restricted air-sea gas exchange from sea-ice expansion, and deepening of remineralization due to seawater cooling, leads to AOU increasing by 37.3 mmol $m^{-3}$ in the deep ocean (Table 2). In the deep North Atlantic, the simulated water mass age is older in the LGM than in PI by up to 500 years, suggesting reduced ventilation (Fig. 7f). Therefore, significant AOU increases are found there (Fig. 7c). Meanwhile, in the SO and deep Pacific Ocean, an increase in ventilation tends to decrease AOU and thus partly cancels out the increase in AOU. As for the effects of iron fertilization and nutrient inventory, EP changes associated with iron fertilization and increase in nutrient inventory enhance biological oxygen consumption and thus increase AOU by 21.4 and 14.1 mmol $m^{-3}$ in the deep ocean, respectively (Table2 and Fig. 7d,e). In particular, glaciogenic dust causes an increase in AOU of 19.8 mmol $m^{-3}$. Our results demonstrate that in addition to climate change, enhanced biological oxygen consumption associated with iron fertilization and increased nutrient inventory are crucial drivers of glacial deoxygenation in the deep ocean. While some previous modelling studies show deep ocean oxygenation during the LGM (Buchanan et al., 2016; Galbraith and Lavergne, 2018), this study and some other studies reproduce deep ocean deoxygenation (Galbraith and Jaccard, 2015; Bopp et al., 2017). The conflicting oxygen change between the previous simulations can be attributed to different treatments of enhanced biological oxygen consumption because iron fertilization and increased nutrient inventory are not considered in these simulations which fail to reproduce deep deoxygenation (Buchanan et al., 2016; Galbraith and Lavergne, 2018).

Glacial oxygen change expands the volume of hypoxic waters (defined here as $[O_2]$ <80 mmol $m^{-3}$) below 1000 m, so that the simulated global volume of hypoxic waters increases from the present value of 120 $Mkm^3$ to 237 $Mkm^3$ in LGM_all. Significant expansion occurs in the deep Pacific and Indian Ocean (Fig. 8), with hypoxic waters also appearing in the upper SO in the Pacific sector, which is consistent with proxy records (Hoogakker et al., 2018; Lu et al., 2016). Since hypoxic conditions are lethal for more than half of marine benthic animals (Vaquer-Sunyer and Duarte, 2008), expansion of hypoxic

water in the deep ocean could have an adverse impact on benthic fauna. The biotic responses to glacial expansion of hypoxic water would be helpful for understanding the biotic response to future deoxygenation associated with global warming.

Finally, we discuss underestimation of deoxygenation in the deep SO in LGM_all. Since simulated changes in the biological pump and sea-ice distributions are consistent with reconstructions (Obase et al., 2017), we turn our attention to changes in circulation. The simulated water mass age of the deep SO is younger in the LGM than in the PI by ~200 years (Fig. 7f), indicating an increase in ventilation. However, $\Delta^{14}C$ records show an increase in water mass age by more than 1000 years, and thus increased stratification (Skinner et al., 2010; Burke and Robinson, 2012). Enhanced mixing of surface waters with deep waters supplies oxygen-rich surface waters into the deep ocean and simultaneously releases carbon accumulated in the deep water to the atmosphere. Therefore, we attribute the underestimation of deoxygenation and carbon accumulation in deep SO to overestimated ventilation. Our results suggest that the stratified SO is required for reproducing glacial $CO_2$ drawdown and oxygen decline in the deep SO, which is consistent with the recent paleo-proxy data and model (Sigman et al., 2010; Kobayashi et al., 2015; Fischer et al., 2010).

## 4 Conclusion and remarks

We quantify impacts on glacial deoxygenation and $CO_2$ decrease caused by glaciogenic dust with higher iron solubility and increase in nutrient inventory associated with sea-level drop, using the coupled atmosphere–ocean general circulation model, aerosol model, and ocean biogeochemical model. As a result, we successfully reproduced the magnitude and large-scale pattern of the observed oxygen change between present and LGM. In conclusion, our results find that the enhanced efficiency of the biological pump is responsible for glacial $CO_2$ decline of more than 30 ppm and approximately half of deep ocean deoxygenation. These results also demonstrate the usefulness of the quantitative model-proxy comparison of oxygen change for understanding glacial-interglacial $CO_2$ change. However, large uncertainty remains, due to the limited number of proxy data of quantitative oxygen change. Thus, we anticipate our findings would encourage studies to gain further qualitative and quantitative reconstructions from throughout the global deep ocean. The comparison between model and other proxy data (e.g.,

$\delta^{13}C$, (Schmittner and Somes, 2016)) is also required to obtain a more robust and comprehensive understanding of the glacial carbon cycle.

We focus on the impacts of changes in DFe flux from the dust on the glacial $CO_2$ drawdown and deoxygenation in this study. However, changes in the sedimentary and hydrothermal DFe flux and ligand concentration that are not considered in this study could be also important. Glacial sea-level drop decreases the sedimentary DFe flux due to the reduction in continental shelves. On the other hand, the hydrothermal DFe flux is increased by lower sea level and bottom pressure (Middleton et al., 2016). Muglia et al (2017) show that the changes in sedimentary and hydrothermal DFe flux associated with sea-level drop increase $CO_2$ by 15 ppm and decrease $CO_2$ by 6ppm, respectively. Although sedimentary DFe flux is proportional to the organic carbon flux reaching the seafloor in our model, a parametrization with Dfe flux as a function of organic carbon flux and bottom oxygen concentrations is proposed in Dale et al (2015). Glacial deep-water deoxygenation would increase sedimentary DFe flux, leading to further $CO_2$ decrease through biological pump. Ligand concentrations strongly control DFe concentrations (Gledhill and Buck, 2012). Because ligand concentration is affected by numerous factors (Völker and Tagliabue, 2015), changes in ligand concentration from PI to LGM have large uncertainty. Thus, we quantify the effect of changes in DFe flux under constant ligand concentration in the PI and LGM simulations. Changes in sedimentary and hydrothermal DFe flux and ligand concentration should be the subject of future research.

Our model-proxy comparison shows the importance of the combination of more sluggish SO circulation and enhanced biological transport of organic matter for the greater accumulation of respired carbon and deoxygenation in the deep SO. However, present climate models cannot reproduce the stratified SO. A possible reason is that the climate models are too coarse to capture the process of dense water formation on the Antarctic shelf and tend to underestimate the strength of stratification in the SO (Heuzé et al., 2013). The brine rejection process and/or change in the vertical diffusion coefficient could be necessary to reproduce the stratified SO (Kobayashi et al., 2015; Bouttes et al., 2011). Similar to glacial oxygen changes, changes in ocean circulation in the SO are crucial for projecting future oxygen changes associated with global

warming (Yamamoto et al., 2015). Therefore, the understanding of glacial oxygen changes will help us to better understand and predict future oxygen changes.

**Acknowledgements**

This work was supported by the Integrated Research Program for Advancing Climate Models from the Ministry of Education, Culture, Sports, Science and Technology, Japan, and JSPS KAKENHI grant number 17H06323. The simulations with the offline biogeochemical model were performed using the Fujitsu PRIMEHPC FX10 system in the Information Technology Center, University of Tokyo.

**References**

Albani, S., Mahowald, N. M., Perry, A. T., Scanza, R. A., Zender, C. S., Heavens, N. G., Maggi, V., Kok, J. F., and Otto-Bliesner, B. L.: Improved dust representation in the Community Atmosphere Model., J. Adv. Model. Earth Sy., 6, 541–570, https://doi.org/10.1002/2013ms000279, 2014.

Bopp, L., Kohfeld, K. E., and Le Qu´er´e, C.: Dust impact on marine biota and atmospheric $CO_2$ during glacial periods, Paleoceanography, 18, 1046, doi:10.1029/2002PA000810, 2003.

Bopp, L., Resplandy, L., Orr, J. C., Doney, S. C., Dunne, J. P., Gehlen, M., Halloran, P., Heinze, C., Ilyina, T., Séférian, R., Tjiputra, J., and Vichi, M.: Multiple stressors of ocean ecosystems in the 21st century: projections with CMIP5 models, Biogeosciences, 10, 6225–6245, https://doi.org/10.5194/bg-10-6225-2013, 2013.

Bopp, L., Resplandy, L., Untersee, A., Le Mezo, P., and Kageyama, M.: Ocean (de)oxygenation from the Last Glacial Maximum to the twenty-first century: insights from Earth System models, Philos. T. Roy. Soc. Lond. A, 375, 2102, https://doi.org/10.1098/rsta.2016.0323, 2017.

Bouttes, N., Paillard, D., Roche, D. M., Brovkin, V., and Bopp, L.: Last Glacial Maximum CO2 and _13C successfully reconciled, Geophys. Res. Lett., 38, L02705, doi:10.1029/2010gl044499, 2011.

Braconnot, P., Otto-Bliesner, B., Harrison, S., Joussaume, S., Peterchmitt, J.-Y., Abe-Ouchi, A., Crucifix, M., Driesschaert, E., Fichefet, Th., Hewitt, C. D., Kageyama, M., Kitoh, A., Laîné, A., Loutre, M.-F., Marti, O., Merkel, U., Ramstein, G., Valdes, P., Weber, S. L., Yu, Y., and Zhao, Y.: Results of PMIP2 coupled simulations of the Mid-Holocene and

Last Glacial Maximum – Part 1: experiments and large-scale features, Clim. Past, 3, 261–277, doi:10.5194/cp-3-261-2007, 2007.

Broecker, W. S.: Glacial to interglacial changes in ocean chemistry, Progress in Oceanography, 11, 151–197, doi:10.1016/0079-6611(82)90007-6, 1982.

Brovkin, V., Ganopolski, A., Archer, D., and Munhoven, G.: Glacial $CO_2$ cycle as a succession of key physical and biogeochemical processes, Clim. Past, 8, 251-264, https://doi.org/10.5194/cp-8-251-2012, 2012.

Buchanan, P. J., Matear, R. J., Lenton, A., Phipps, S. J., Chase, Z., and Etheridge, D. M.: The simulated climate of the Last Glacial Maximum and insights into the global marine carbon cycle, Clim. Past, 12, 2271-2295, https://doi.org/10.5194/cp-12-2271-2016, 2016.

Bunzel, D., Schmiedl, G., Lindhorst, S., Mackensen, A., Reolid, J., Romahn, S., and Betzler, C.: A multi-proxy analysis of Late Quaternary ocean and climate variability for the Maldives, Inner Sea, Clim. Past, 13, 1791-1813, https://doi.org/10.5194/cp-13-1791-2017, 2017.

Burke, A. and Robinson, L. F.: The Southern Ocean's role in carbon exchange during the last deglaciation, Science, 335, 557–561, 2012.

Chikamoto, M. O., Abe-Ouchi, A., Oka, A., Ohgaito, R., and Timmermann, A.: Quantifying the ocean's role in glacial $CO_2$ reductions, Clim. Past, 8, 545-563, https://doi.org/10.5194/cp-8-545-2012, 2012.

Ciais, P., Sabine, C., Bala, G., Bopp, L., Brovkin, V., Canadell, J., Chhabra, A., DeFries, R., Galloway, J., Heimann, M., Jones, C., Le Quéré, C., Myneni, R. B., Piao, S., and Thornton, P.: Carbon and Other Biogeochemical Cycles, in: Climate Change 2013: The Physical Science Basis. Contribution of Working Group I to the Fifth Assessment Report of the Intergovernmental Panel on Climate Change, edited by: Stocker, T. F., Qin, D., Plattner, G.-K., Tignor, M., Allen, S. K., Boschung, J., Nauels, A., Xia, Y., Bex, V., and Midgley, P. M., Cambridge University Press, Cambridge, United Kingdom and New York, NY, USA, 465– 570, 2013.

Conway, T., Wolff, E., Roethlisberger, R., Mulvaney, R., and Elderfield, H.: Constraints on soluble aerosol iron flux to the Southern Ocean at the Last Glacial Maximum, Nature Communications, 6, 1–9, doi:10.1038/ncomms8850, 2015.

Curry,W. B. and Oppo, D.W.: Glacial water mass geometry and the distribution of $\delta^{13}C$ of $CO_2$ in the western Atlantic Ocean, Paleoceanography, 20, PA1017, doi:10.1029/2004PA001021, 2005.

Diaz, R. J. and Rosenberg, R.: Spreading dead zones and consequences for marine ecosystems, Science, 321, 926–929, 2008.

Durand, A.,Chase, Z., Noble, T. L., Bostock, H., Jaccard, S. L., Townsend, A. T., Bindoff, N. L., Neil, H., and Jacobsen, G.: Reduced oxygenation at intermediate depth of the southwest Pacific during the last glacial maximum, Earth Planet. Sc. Lett., 491, 48-57, 2018.

Eppley, R. W.: Temperature and phytoplankton growth in the sea, Fish. B.-NOAA, 70, 1063–1085, 1972.

Fischer, H., Schmitt, J., Luthi, D., Stocker, T. F., Tschumi, T., Parekh, P., Joos, F., Kohler, P., Volker, C., Gersonde, R., Barbante, C., Le Floch, M., Raynaud, D., and Wolff, E.: The role of Southern Ocean processes in orbital and millennial CO2 variations – a synthesis, Quaternary Sci. Rev., 29, 193–205, 2010.

Galbraith, E. and de Lavergne, C.: Response of a comprehensive climate model to a broad range of external forcings: relevance for deep ocean ventilation and the development of late Cenozoic ice ages, Clim. Dynam., https://doi.org/10.1007/s00382-018-4157-8, 2018.

Galbraith, E. D. and Jaccard, S. L.: Deglacial weakening of the oceanic soft tissue pump: global constraints from sedimentary nitrogen isotopes and oxygenation proxies, Quaternary Sci. Rev., 109, 38–48, doi:10.1016/j.quascirev.2014.11.012, 2015.

Garcia, H. E., Locarnini, R., Boyer, T., Antonov, J., Baranova, O., Zweng, M., and Johnson, D.: Volume 3: Dissolved Oxygen, Apparent Oxygen Utilization, and Oxygen Saturation,World Ocean Atlas 2009, S. Levitus, Ed. NOAA Atlas NESDIS 70, US Government Printing Office, Washington, DC, 344 pp., 2010a.

Garcia, H. E., Locarnini, R., Boyer, T., Antonov, J., Zweng, M., Baranova, O., and Johnson, D.: Volume 4: Nutrients (phosphate, nitrate, silicate), World Ocean Atlas 2009, edited by: Levitus, S., NOAA Atlas NESDIS 71, US Government Printing Office, Washington, DC, 398 pp., 2010b.

Gledhill, M. and Buck, K.: The organic complexation of iron in the marine environment: a review, Frontiers in Microbiology, 3, 1–17, doi:10.3389/fmicb.2012.00069, 2012.

Gottschalk, J., Skinner, L. C., Lippold, J., Vogel, H., Frank, N., Jaccard, S. L., and Waelbroeck, C.: Biological and physical controls in the Southern Ocean on past millennial-scale atmospheric CO2 changes, Nat. Commun., 7, 11539, doi:10.1038/ncomms11539,2016.

Heuzé, C., Heywood, K. J., Stevens, D. P., and Ridley, J. K.: Southern Ocean bottom water characteristics in CMIP5 models, Geophys. Res. Lett., 40, 1409–1414, doi:10.1002/grl.50287, 2013.

Hoogakker, B. A. A., Elderfield, H., Schmiedl, G., McCave, I. N., and Rickaby, R. E. M.: Glacial–interglacial changes in bottom water oxygen content on the Portuguese margin, Nat. Geosci., 8, 40–43, doi:10.1038/ngeo2317, 2015.

Hoogakker, B. A. A., Lu, Z., Umling, N., Jones, L., Zhou, X., Rickaby, R. E. M., Thunell, R., Cartapanis, O., and Galbraith, E.: Glacial expansion of oxygen-depleted seawater in the eastern tropical Pacific. Nature, 562 (7727), 410-413. 10.1038/s41586-018-0589-x, 2018.

Ito, A., Myriokefalitakis, S., Kanakidou, M., Mahowald, N. M., Scanza, R. A., Hamilton, D. S., Baker, A. R., Jickells, T., Sarin, M., Bikkina, S., Gao, Y., Shelley, R. U., Buck, C. S., Landing, W. M., Bowie, A. R., Perron, M. M. G., Guieu, C., Meskhidze, N., Johnson, M. S., Feng, Y., Kok, J. F., Nenes, A., and Duce, R. A.: Pyrogenic iron: The missing link to high iron solubility in aerosols, Sci. Adv., in review, 2019.

Ito, T. and Follows, M. J.: Preformed phosphate, soft tissue pump and atmospheric $CO_2$, J. Mar. Res., 63, 813–839, 2005.

Jaccard, S. L. and Galbraith, E. D.: Large climate-driven changes of oceanic oxygen concentrations during the last deglaciation, Nat. Geosci., 5, 151–156, doi:10.1038/ngeo1352, 2012.

Jaccard, S. L., Hayes, C. T., Hodell, D. A., Anderson, R. F., Sigman, D. M., and Haug, G. H.: Two modes of change in Southern Ocean productivity over the past million years, Science, 339, 1419–1423, 2013.

Key, R. M., Kozyr, A., Sabine, C. L., Lee, K., Wanninkhof, R., Bullister, J. L., Feely, R. A., Millero, F. J., Mordy, C., and Peng, T.-H.: A global ocean carbon climatology: Results from Global Data Analysis Project (GLODAP), Global Biogeochem. Cy., 18, GB4031, https://doi.org/10.1029/2004GB002247, 2004.

Kobayashi, H., Abe-Ouchi, A., and Oka, A.: Role of Southern Ocean stratification in glacial atmospheric CO2 reduction evaluated by a three-dimensional ocean general circulation model, Paleoceanography, 30, 1202–1216, 2015.

Kobayashi, H., and Oka, A.: Response of atmospheric $pCO_2$ to glacial changes in the Southern Ocean amplified by carbonate compensation. Paleoceanography 33, 1206-1229, 2018.

Kohfeld, K. E., Le Quéré, C., Harrison, S. P., and Anderson, R. F.: Role of marine biology in glacial-interglacial CO2 cycles, Science, 308, 74–78, doi:10.1126/science.1105375, 2005.

Kohfeld, K. E., Graham, R. M., De Boer, A. M., Sime, L. C., Wolff, E. W., Le Quere, C., and Bopp, L.: Southern Hemisphere westerly wind changes during the Last Glacial Maximum: paleo-data synthesis, Quaternary Sci. Rev., 68, 76–95, https://doi.org/10.1016/j.quascirev.2013.01.017, 2013.

Lambert, F., Tagliabue, A., Shaffer, G., Lamy, F., Winckler, G., Farias, L., Gallardo, L., and De Pol-Holz, R.: Dust fluxes and iron fertilization in Holocene and Last Glacial Maximum climates, Geophys. Res. Lett., 42, 6014–6023, doi:10.1002/2015gl064250, 2015.

Lu, Z., Hoogakker, B. A. A., Hillenbrand, C.-D., Zhou, X., Thomas, E., Gutchess, K. M., Lu, W., Jones, L., and Rickaby, R. E. M.: Oxygen depletion recorded in upper waters of the glacial Southern Ocean, Nat. Commun., 7, 11146, https://doi.org/10.1038/ncomms11146, 2015.

Mahowald, N. M., Muhs, D. R., Levis, S., Rasch, P. J., Yoshioka, M., Zender, C. S., and Luo, C.: Change in atmospheric mineral aerosols in response to climate: last glacial period, preindustrial, modern, and doubled carbon dioxide climates, J. Geophys. Res., 111, D10202, doi:10.1029/2005JD006653, 2006.

Marinov, I., Gnanadesikan, A., Sarmiento, J. L., Toggweiler, J. R., Follows, M., and Mignone, B. K.: Impact of oceanic circulation on biological carbon storage in the ocean and atmospheric pCO2, Global Biogeochem. Cy. 22(3), GB3007, doi:10.1029/2007GB002958, 2008.

Martin, J. H.: Glacial-interglacial CO2 change: the iron hypothesis, Paleoceanography, 5, 1–13, 1990.

Matsumoto, K.: Biology-mediated temperature control on atmospheric $pCO_2$ and ocean biogeochemistry, Geophys. Res. Lett., 34, L20605, https://doi.org/10.1029/2007GL031301, 2007.

Middleton, J. L., Langmuir, C. H., Mukhopadhyay, S., McManus, J. F., and Mitrovica, J. X.: Hydrothermal iron flux variability following rapid sea level changes, Geophys. Res. Lett., 43, 3848–3856, https://doi.org/10.1002/2016GL068408, 2016.

Moore, J. K. and Braucher, O.: Sedimentary and mineral dust sources of dissolved iron to the world ocean, Biogeosciences, 5, 631–656, doi:10.5194/bg-5-631-2008, 2008.

Moore, C. M., Mills, M. M., Arrigo, K. R., Berman-Frank, I., Bopp, L., Boyd, P. W., Galbraith, E. D., Geider, R. J., Guieu, C., Jaccard, S. L., Jickells, T. D., La Roche, J., Lenton, T. M., Mahowald, N. M., Marañón, E., Marinov, I., Moore, J. K., Nakatsuka, T., Oschilles, A., Saito, M. A., Thingstad, T. F., Tsuda, A., and Ulloa, O.: Processes and patterns of oceanic nutrient limitation, Nat. Geosci., 6, 701–710,https://doi.org/10.1038/ngeo1765, 2013.

Muglia, J., Somes, C., Nickelsen, L., and Schmittner, A.: Combined effects of atmospheric and seafloor iron fluxes to the glacial ocean. Paleoceanography 32, 1204–1218, 2017.

Obase, T., Abe-Ouchi, A., Kusahara, K., Hasumi, H., and Ohgaito, R.: Responses of basal melting of Antarctic ice shelves to the climatic forcing of the Last Glacial Maximum and $CO_2$ doubling. J. Climate, 30, 3473–3497, 2017.

Ohgaito, R., Abe-Ouchi, A., O'ishi, R., Takemura, T., Ito, A., Hajima, T., Watanabe, S., and Kawamiya, M.: Effect of high dust amount on surface temperature during the Last Glacial Maximum: a modelling study using MIROC-ESM, Clim. Past, 14, 1565-1581, https://doi.org/10.5194/cp-14-1565-2018, 2018.

Oka, A., Abe-Ouchi, A., Chikamoto, M. O., and Ide, T.: Mechanisms controlling export production at the LGM: Effects of changes in oceanic physical field and atmospheric dust deposition, Global Biogeochem. Cy., 25, GB2009, doi:10.1029/2009GB003628, 2011.

Parekh, P., Follows, M. J., and Boyle, E. A.: Decoupling of iron and phosphate in the global ocean, Global Biogeochem. Cy., 19, GB2020, doi:10.1029/2004GB002280, 2005.

Parekh, P., Follows, M. J., Dutkiewicz, S., and Ito, T.: Physical and biological regulation of the soft tissue carbon pump, Paleoceanography, 21, PA3001, doi:10.1029/2005PA001258, 2006.

Sarmiento, J. L., and Gruber, N.: Ocean Biogeochemical Dynamics, chap. 8, Carbon cycle, pp.318-358, Princeton Univ. Press, Princeton, N. J, 2006.

Schmiedl, G. and Mackensen, A.: Multispecies stable isotopes of benthic foraminifers reveal past changes of organic matter decomposition and deepwater oxygenation in the Arabian Sea, Paleoceanography, 21, 1–14, doi:10.1029/2006PA001284, 2006.

Schmittner, A. and Somes, C. J.: Complementary constraints from carbon (C-13) and nitrogen (N-15) isotopes on the glacial ocean's soft-tissue biological pump, Paleoceanography, 31, 669–693, 2016.

Schroth, A. W., Crusius, J., Sholkovitz, E. R., and Bostick, B. C.: Iron solubility driven by speciation in dust sources to the ocean, Nat. Geosci., 2, 337–340, 2009.

Shoenfelt, E. M., Winckler, G., Lamy, F., Anderson, R. F., and Bostick, B. C.: Highly bioavailable dust-borne iron delivered to the Southern Ocean during glacial periods. Proc. Natl. Acad. Sci. USA, 115, 11180-11185, 2018

Sigman, D. M., Hain, M. P., and Haug, G. H.: The polar ocean and glacial cycles in atmospheric $CO_2$ concentration, Nature, 466, 47–55, doi:10.1038/nature09149, 2010.

Skinner, L. C., Fallon, S., Waelbroeck, C., Michel, E., and Barker, S.: Ventilation of the deep Southern Ocean and deglacial CO2 rise, Science, 328, 1147–1151, 2010.

Tagliabue, A., Bopp, L., Dutay, J. C., Bowie, A. R., Chever, F., Jean-Baptiste, P., Bucciarelli, E., Lannuzel, D., Remenyi, T., Sarthou, G., Aumont, O., Gehlen, M., and Jeandel, C.: Hydrothermal contribution to the oceanic dissolved iron inventory, Nat. Geosci., 3, 252–256, 2010.

Tagliabue, A., Bopp, L., Roche, D. M., Bouttes, N., Dutay, J.-C., Alkama, R., Kageyama, M., Michel, E., and Paillard, D.: Quantifying the roles of ocean circulation and biogeochemistry in governing ocean carbon-13 and atmospheric carbon dioxide at the last glacial maximum, Clim. Past, 5, 695-706, https://doi.org/10.5194/cp-5-695-2009, 2009.

Umling, N. E., and Thunell, R. C.: Mid-depth respired carbon storage and oxygenation of the eastern equatorial Pacific over the last 25,000 years. Quaternary Science Reviews, 189, 43-56, 2018.

Vaquer-Sunyer, R. and Duarte, C. M.: Thresholds of hypoxia for marine biodiversity, Proc. Natl. Acad. Sci., 105, 15452–57, 2008.

Völker, C. and Tagliabue, A.: Modeling organic iron-binding ligands in a three-dimensional biogeochemical ocean model, Mar. Chem., 173, 67–77, doi:10.1016/j.marchem.2014.11.008, 2015.

Wallmann, K., Schneider, B., and Sarnthein, M.: Effects of eustatic sea-level change, ocean dynamics, and nutrient utilization on atmospheric $pCO_2$ and seawater composition over the last 130 000 years: a model study, Clim. Past, 12, 339-375, https://doi.org/10.5194/cp-12-339-2016, 2016.

Yamamoto, A., Abe-Ouchi, A., Shigemitsu, M., Oka, A., Takahashi, K., Ohgaito, R., and Yamanaka, Y.: Global deep ocean oxygenation by enhanced ventilation in the Southern Ocean under longterm global warming, Global Biogeochem. Cy., 29, 1801–1815, 2015.

Yamamoto, A., Abe-Ouchi, A., and Yamanaka, Y.: Long-term response of oceanic carbon uptake to global warming via physical and biological pumps, Biogeosciences, 15, 4163-4180, https://doi.org/10.5194/bg-15-4163-2018, 2018.

Clim. Past Discuss., https://doi.org/10.5194/cp-2019-31
Manuscript under review for journal Clim. Past
Discussion started: 7 March 2019


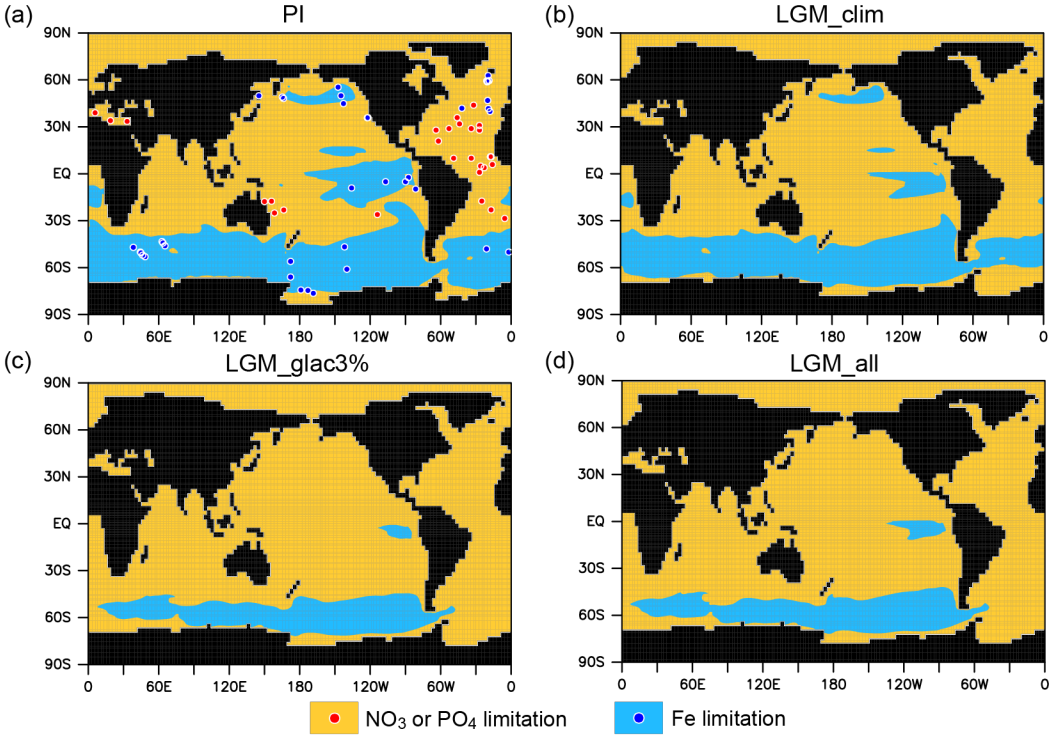


**Figure 1.** Primary limiting nutrient for phytoplankton for (a) PI, (b) LGM_clim. (c)LGM_glac3%, and (d) LGM_all. Shade indicates $NO_3$ or $PO_4$ limitation (orange) and Fe limitation (blue). Circles represent observed limiting nutrients from nutrient addition experiments (Moore et al., 2013).

Clim. Past Discuss., https://doi.org/10.5194/cp-2019-31
Manuscript under review for journal Clim. Past
Discussion started: 7 March 2019


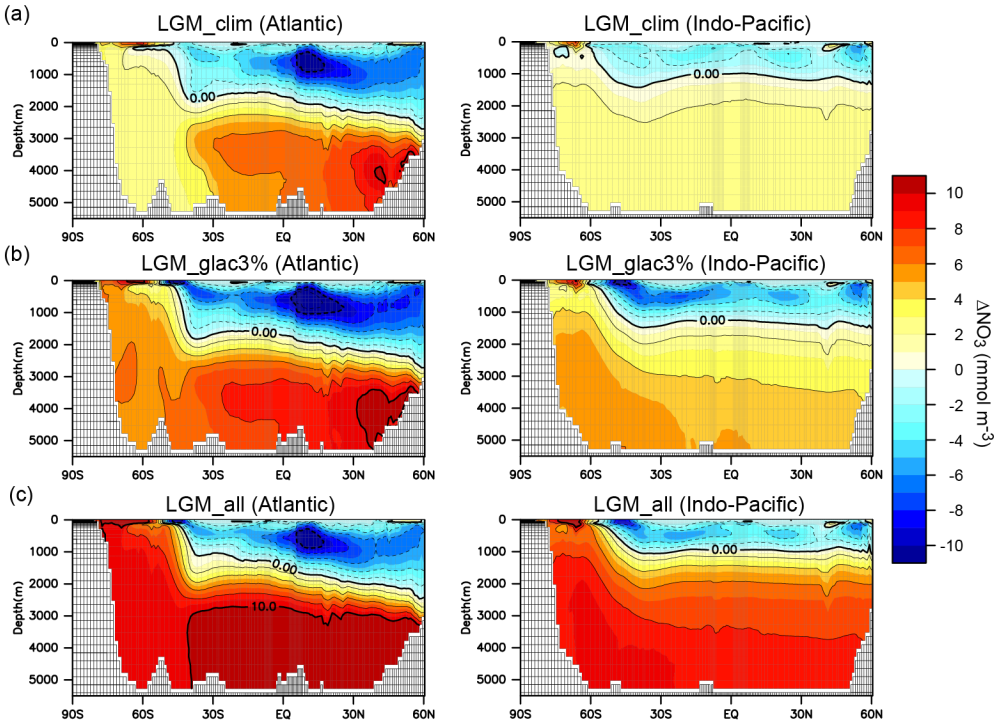


**Figure 2.** $NO_3$ change due to changes in climate and biological pump in LGM simulations. Zonal mean changes in $NO_3$ from PI to (a) LGM_clim, (b) LGM_glac3%, and (c) LGM_all. The left and right panels show the Atlantic and Indo-Pacific oceans, respectively.

Clim. Past Discuss., https://doi.org/10.5194/cp-2019-31
Manuscript under review for journal Clim. Past
Discussion started: 7 March 2019


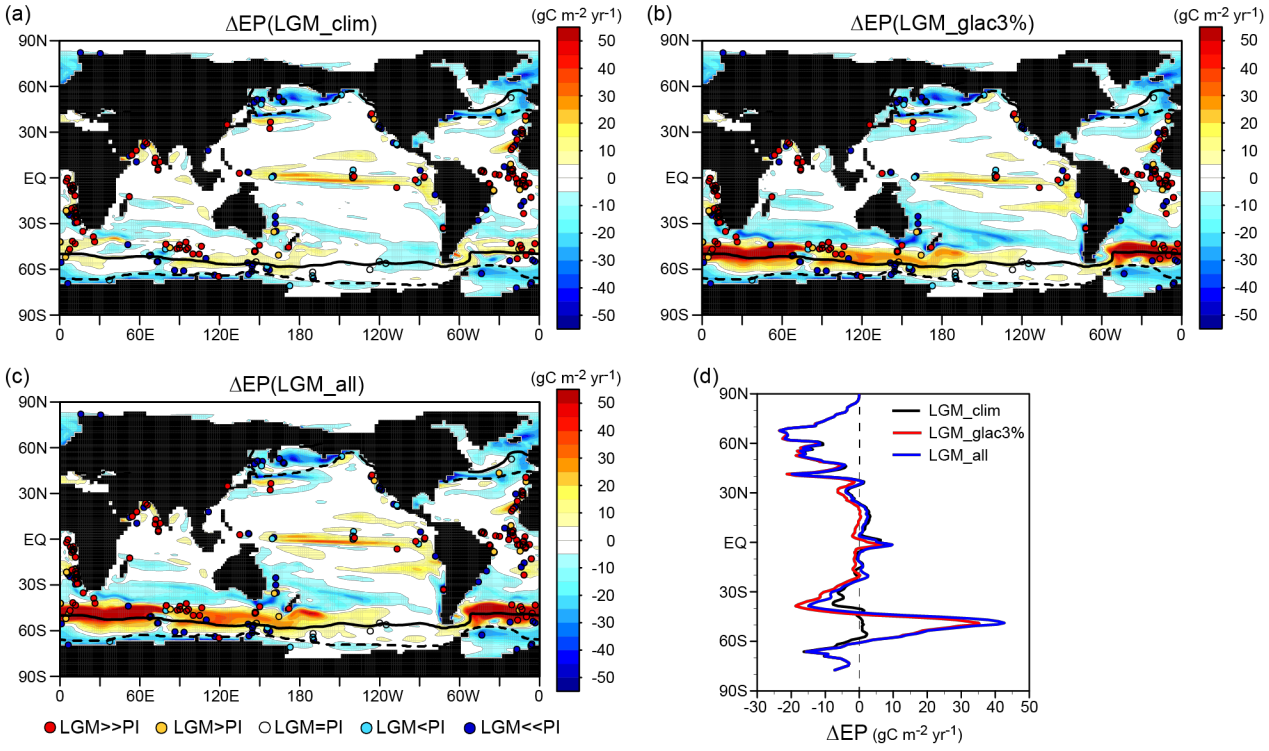


**Figure 3.** Model-proxy comparison of EP change from the PI to LGM. EP difference from the PI for (a) LGM_clim, (b) LGM_glac3%, and (c) LGM_all. Circles show proxy data (Kohfeld et al., 2005). Solid (dotted) lines refer to the glacial sea ice fraction of 0.1 in August (February). (d) Zonal mean changes in surface EP from the PI for LGM_clim (black), LGM_glac3% (red), and LGM_all (blue).

Clim. Past Discuss., https://doi.org/10.5194/cp-2019-31
Manuscript under review for journal Clim. Past
Discussion started: 7 March 2019


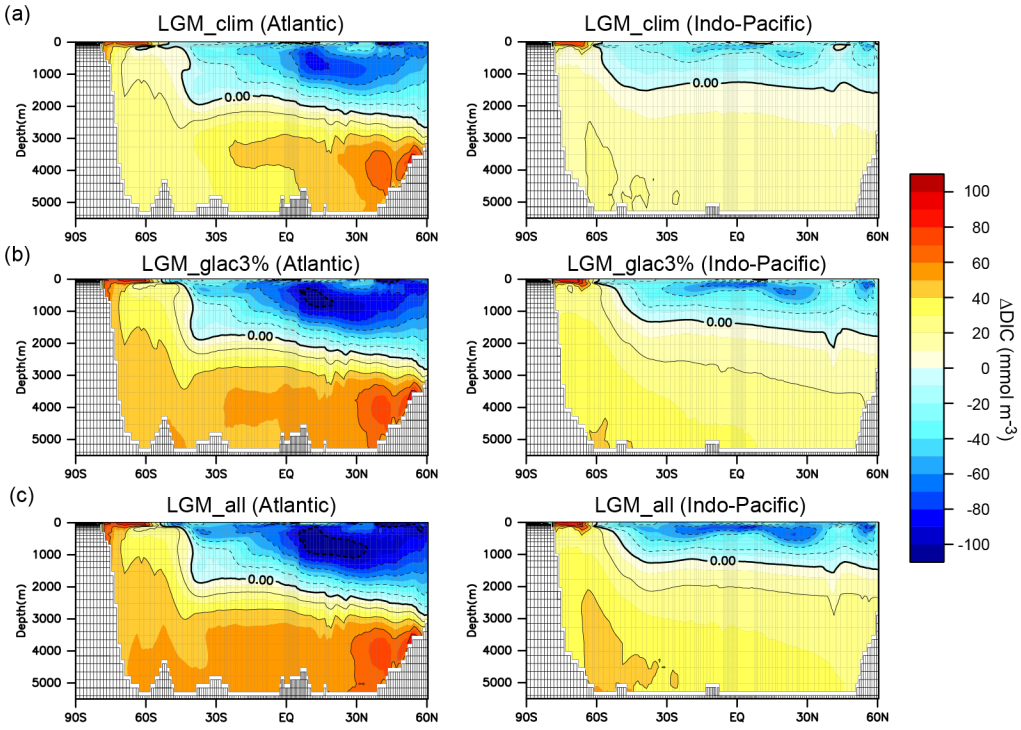


**Figure 4.** DIC change due to changes in climate and biological pump in LGM simulations. Zonal mean changes in DIC from PI to (a) LGM_clim, (b) LGM_glac3%, and (c) LGM_all. The left and right panels show the Atlantic and Indo-Pacific oceans, respectively.

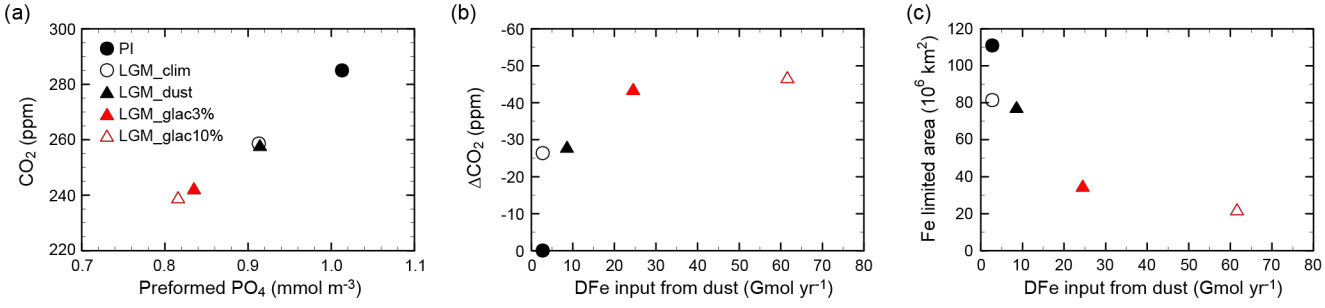


**Figure 5.** $CO_2$ change and its relationship to efficiency of the biological pump and iron cycle. (a) Atmospheric $CO_2$ as a function of globally averaged preformed $PO_4$. (b) Changes in $CO_2$ from PI as a function of DFe input from dust. (c) Fe limited area as a function of DFe input from dust. Shown are PI (black filled circle), LGM_clim (black open circle), LGM_dust (black filled triangle), LGM_glac3% (red filled triangle), and LGM_glac10% (red open triangle).

Clim. Past Discuss., https://doi.org/10.5194/cp-2019-31
Manuscript under review for journal Clim. Past
Discussion started: 7 March 2019


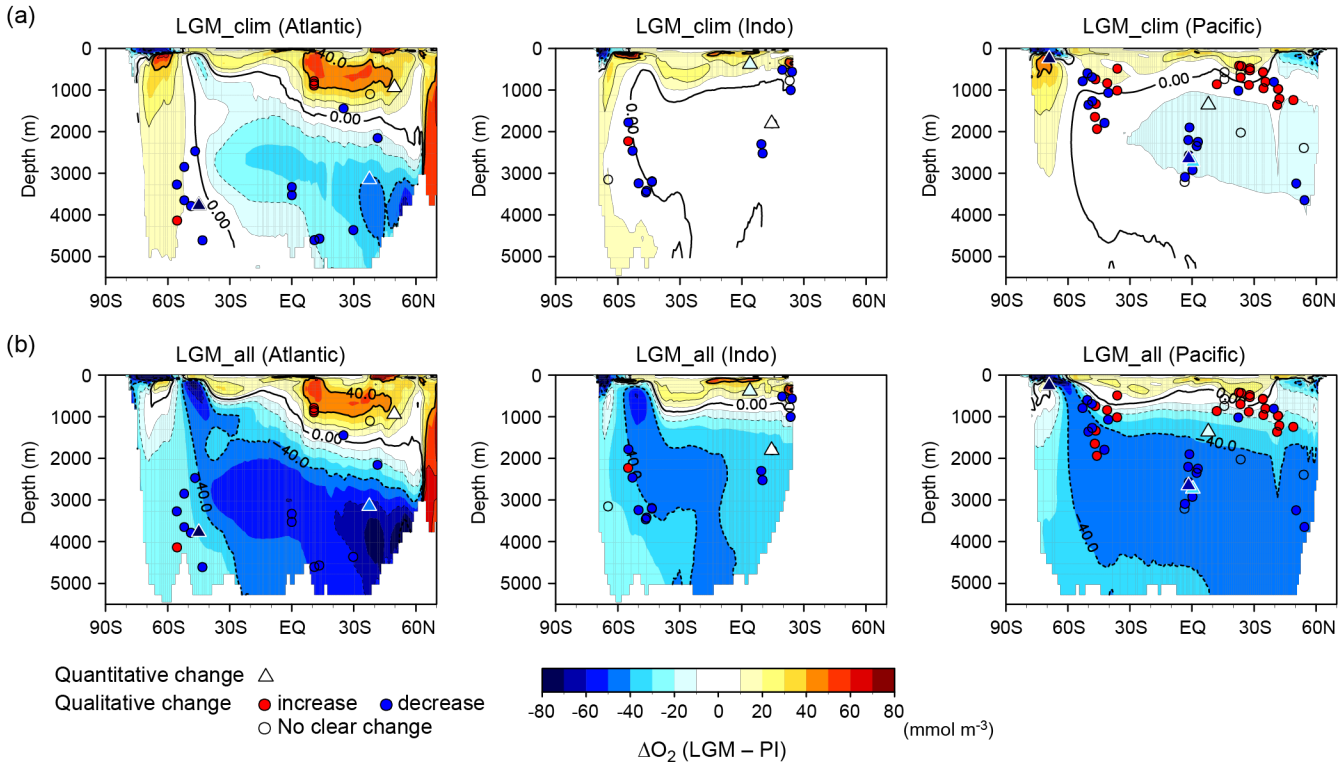


**Figure 6.** Model-proxy comparison of changes in dissolved oxygen concentration from the PI to LGM. Zonal mean changes in $O_2$ from PI to (a) LGM_clim and (b) LGM_all for the Atlantic (left), Indian (middle), and Pacific (right) Oceans; contour interval is 20 mmol m$^{-3}$. Circles show proxy records of qualitative $O_2$ change from multi-proxy data compilation from Jaccard and Galbraith (2012) and Durand et al (2018). Red (blue) circles indicate $O_2$ increase (decrease) from the Holocene to LGM. Triangles show proxy records of quantitative $O_2$ change from (Hoogakker et al., 2015, 2018; Gottschalk et al., 2016; Lu et al., 2016; Bunzel et al., 2017; Umling and Thunell, 2018; Schmiedl and Mackensen, 2006) (triangles shaded using the same colour scale).

Clim. Past Discuss., https://doi.org/10.5194/cp-2019-31
Manuscript under review for journal Clim. Past
Discussion started: 7 March 2019


Climate of the Past
Discussions
Open Access
EGU

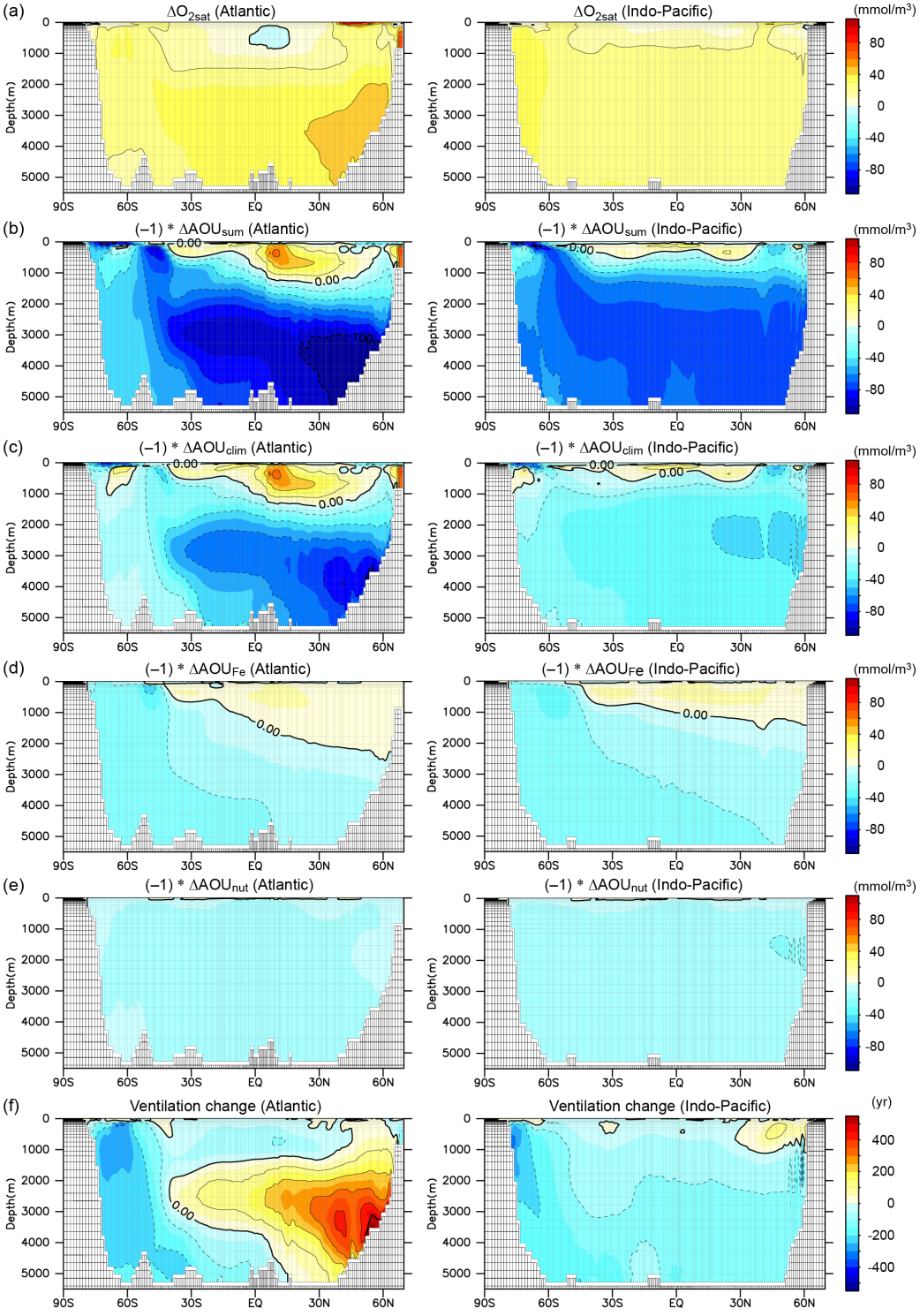

Clim. Past Discuss., https://doi.org/10.5194/cp-2019-31
Manuscript under review for journal Clim. Past
Discussion started: 7 March 2019


**Figure 7.** Contributions of individual mechanisms to oxygen change and ventilation change. Zonal mean changes of (a) $O_{2sat}$, (b) $AOU_{sum}$, (c) $AOU_{clim}$, (d) $AOU_{Fe}$, (e) $AOU_{nut}$, and (f) ventilation age from PI to LGM. Left and right panels show the Atlantic and Indo-Pacific Oceans: contour intervals are 20 mmol $m^{-3}$ for (a)–(e) and 100 years for (f). We decomposed the total AOU change ($\Delta AOU_{sum} = AOU_{(LGM\_all)} - AOU_{(PI)}$) into the effects of climate change ($\Delta AOU_{clim} = AOU_{(LGM\_clim)} - AOU_{(PI)}$), iron fertilization ($\Delta AOU_{Fe} = AOU_{(LGM\_glac3\%)} - AOU_{(LGM\_clim)}$), and increase in nutrient inventory ($\Delta AOUnut = AOU_{(LGM\_all)} - AOU_{(LGM\_glac3\%)}$).

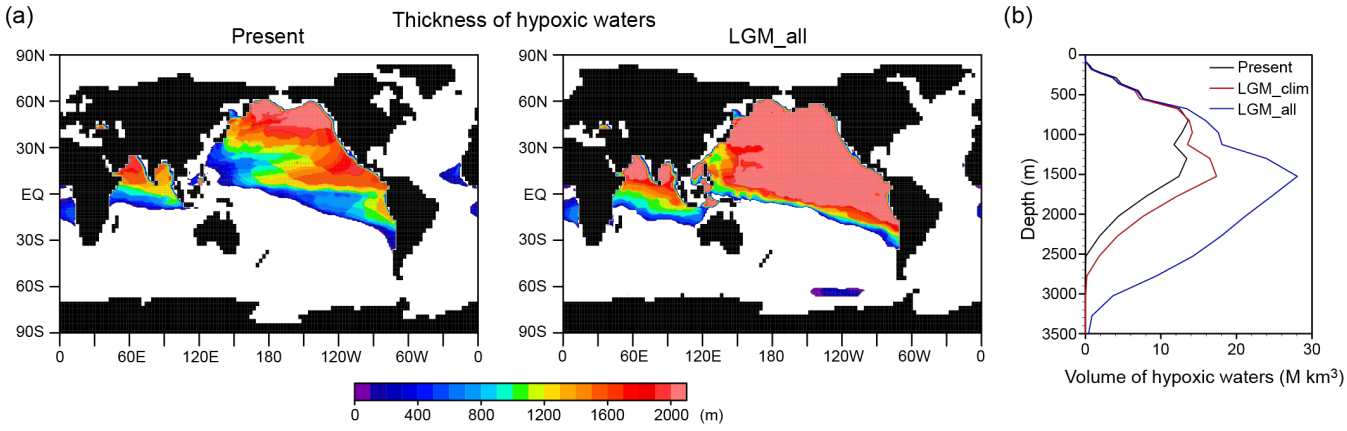


**Figure 8.** Expansion of hypoxic waters. Horizontal distribution of thickness of hypoxic waters ($[O_2]$ <80 mmol $m^{-3}$) for (a) present and (b) LGM_all. (c) Vertical distribution of hypoxic waters for the present (black), LGM_clim (red), and LGM_all (blue). Because present coarse resolution models have difficulties in reproducing low oxygen concentration for the present day (Bopp et al., 2013), observed values from WOA2009 (Garcia et al., 2010a) are used for the present. For the LGM simulations, we combine the observed values with the modelled changes.

Clim. Past Discuss., https://doi.org/10.5194/cp-2019-31
Manuscript under review for journal Clim. Past
Discussion started: 7 March 2019


| Experiments | Climate | Dust deposition | Fe solubility in glaciogenic dust | Dust DFe (Gmol/yr) | Global $PO_4$ (mmol/m$^3$) |
|---|---|---|---|---|---|
| PI | PI | PI | - | 2.7 | 2.13 |
| LGM_clim | LGM | PI | - | 2.7 | 2.2 (+3%) |
| LGM_dust | LGM | LGMctl | - | 8.6 | 2.2 (+3%) |
| LGM_glac3% | LGM | LGMglac | 3% | 24.5 | 2.2 (+3%) |
| LGM_glac10% | LGM | LGMglac | 10% | 61.6 | 2.2 (+3%) |
| LGM_all | LGM | LGMglac | 3% | 24.5 | 2.45 (+15%) |

Table 1. Description of the model experiments.

| Experiments | Surface $NO_3$ (mmol/m$^3$) | Surface DFe (μmol/m$^3$) | Fe limited area ($10^6$ km$^2$) | Global ΔEP (Pg C/yr) | ΔEP (>45°S) (Pg C/yr) | ΔEP (<45°S) (Pg C/yr) | Preformed $PO_4$ (mmol/m$^3$) | $\Delta CO_2$ (ppm) | $\Delta O_{2\,deep}$ (mmo/m$^3$) | $\Delta AOU_{deep}$ (mmol/m$^3$) |
|---|---|---|---|---|---|---|---|---|---|---|
| PI | 7.7 | 0.38 | 111 | (8.54) | (6.19) | (2.35) | 1.013 | (285) | (156) | (182.5) |
| LGM_clim | 6.8 | 0.39 | 81 | -0.54 | -0.45 | -0.09 | 0.913 | -26.4 | -7 | 37.3 |
| LGM_dust | 6.9 | 0.42 | 80 | -0.54 | -0.49 | -0.05 | 0.914 | -27.6 | -8 | 38.9 |
| LGM_glac3% | 5.8 | 0.5 | 35 | -0.54 | -1.31 | +0.77 | 0.835 | -43.2 | -28 | 58.7 |
| LGM_glac10% | 5.5 | 0.54 | 23 | -0.54 | -1.46 | +0.92 | 0.816 | -46.4 | -33 | 63.6 |
| LGM_all | 6.5 | 0.48 | 39 | +0.32 | -0.63 | +0.95 | 1.002 | -59.2 | -42 | 72.8 |

Table 2. Results of the model experiments. Simulated global average of surface $NO_3$, DFe, Fe limited area and changes in export production at 100 m, atmospheric $CO_2$, and globally averaged $O_2$ and AOU below 2000 m depth from the PI. Values in brackets are the results of PI.